

Single Atom Substitution Alters the Polymorphic Transition Mechanism in Organic Electronic Crystals

Hyunjoong Chung,[†] Shanwen Chen,[†] Nikita Sengar,^{‡®} Daniel W. Davies,[†] Guillaume Garbay,[§] Yves H. Geerts, Paulette Clancy, and Ying Diao*

Supporting Information

ABSTRACT: Understanding the molecular mechanism of polymorphic transition is essential for controlling molecular packing for high-performance organic electronics. Polymorphic transition in molecular crystals mostly follows the nucleation and growth mechanism. We recently discovered a cooperative polymorphic transition in organic semiconductor single crystals driven by bulky side-chain rotation. In this work, we demonstrate that a single atom substitution in the side-chains from carbon to silicon can completely alter the transition pathway from a cooperative transition to nucleation and

ditBu-BTBT diTMS-BTBT Cooperative Transition Nucleation and Growth

growth. We reveal that bulkier side-chains become interlocked to inhibit side-chain rotation and thereby hinder molecular cooperativity to lead to the nucleation and growth mechanism. We report the utilities of both types of transitions in organic electronic devices. Nucleation and growth allows kinetic access to metastable polymorphs at ambient conditions for structure property study. On the other hand, cooperative transition enables in situ and reversible access to polymorphs for rapid modulation of electronic properties while maintaining structural integrity. Using this simple molecular design rule, we can access both polymorphic transition pathways and selectively utilize their advantages in organic electronic applications.

Polymorphism¹ is the ability of a compound to adopt multiple crystalline packing states. It is especially prevalent in molecular crystals which exhibit polymorphism at near ambient conditions because of their weak van der Waals and multipole interactions.² According to a study by Cruz-Cabeza and colleagues,³ almost one in two organic compounds display polymorphism. Different polymorphs have distinct physical properties4 and, in the context of organic electronics, the charge carrier mobility between polymorphs can vary by up to several orders of magnitude,⁵ attracting considerable research interest.6-15 Two major roles of polymorphism in organic electronics are as follows: first, it is used as an avenue for enhancing the device performance without changing the chemical structure and, second, it is used as a platform for examining the fundamental relationships between charge transport and crystal structure. However, polymorphs are often discovered serendipitously. It remains challenging to control and access polymorphs in a consistent fashion important for large-area production beyond the laboratory scale. Toward this aim, a molecular-level understanding of the polymorphic transition mechanism and pathways is essential but rarely studied.

Two distinct polymorphic transition mechanisms have been reported before: one that transforms in a molecule-bymolecule fashion 16,17 and the other involving molecular

cooperativity. 18,19 The former, also known as reconstructive transition or nucleation and growth,²⁰⁻²³ experiences significant changes between the "parent" and "daughter" crystal structures that usually disrupt the integrity of the "parent" crystal. The latter, also called a displacive, martensitic, topotactic, or cooperative transition, 24 experiences slight changes and exhibits a close orientational relationship between the parent and daughter crystal structure; such a transition also preserves the structural integrity of the crystal, enabling singlecrystal-to-single-crystal transitions. In our work, we refer to the former mechanism as nucleation and growth and the latter case as cooperative transition. We avoid using terms such as displacive, martensitic transitions, which are directly inherited from metallurgy,²⁵ as we observe richer molecular motions during cooperative transition that cannot be fully captured by these terms. We note that these two polymorphic transition mechanisms are correlated to the relative difference between the polymorph structures, large and small, respectively. However, such correlation does not explain the molecular origin of cooperative behavior. Therefore, in this work, we

Received: August 23, 2019 Revised: October 14, 2019 Published: October 16, 2019

Department of Chemical and Biomolecular Engineering, University of Illinois at Urbana—Champaign, 600 South Mathews Avenue, Urbana, Illinois 61801, United States

Department of Chemical and Biomolecular Engineering, Johns Hopkins University, 3400 North Charles Street, Baltimore, Maryland 21218, United States

[§]Laboratoire de Chimie des Polymères Faculté des Sciences, Université Libre de Bruxelles (ULB), CP206/1, Boulevard du Triomphe, Brussels 1050, Belgium

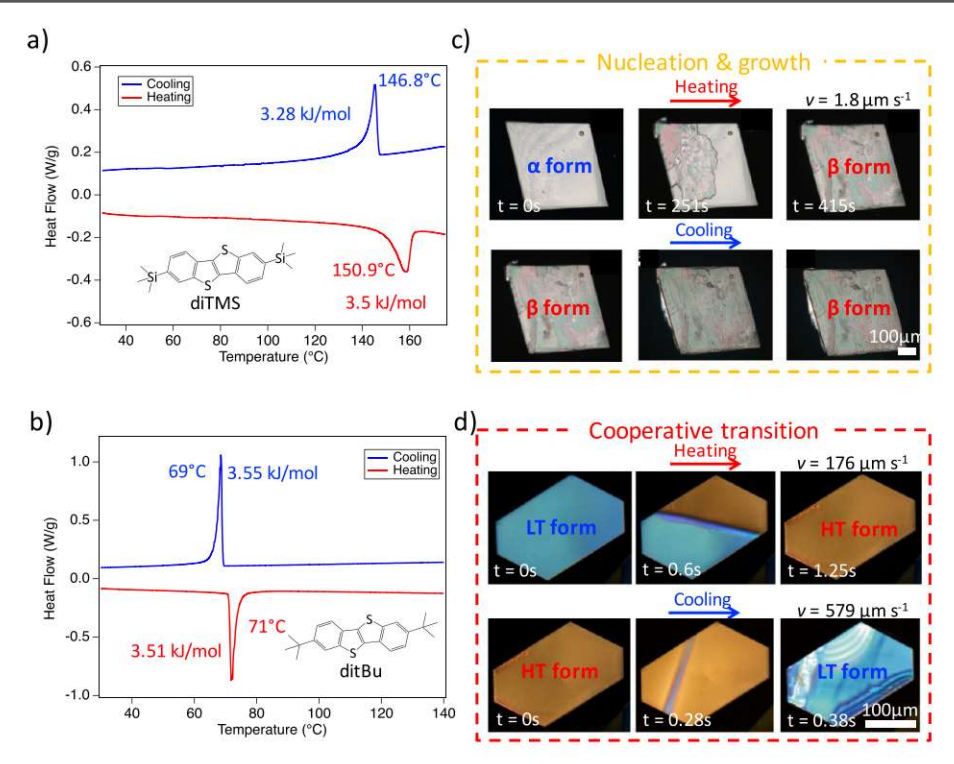


Figure 1. Two polymorphic transition pathways of nucleation and growth and cooperative transition in single crystals of diTMS and ditBu. (a) DSC of diTMS powder showing reversible polymorphic transition. The molecular structure is shown in the inset. (b) DSC of ditBu powder showing reversible polymorphic transition. The molecular structure is shown in the inset. (c) CPOM images of a single crystal of diTMS α form. The α form transitions to the β form upon heating after approximately 415 s. The average growth speed is calculated to be 1.8 μm s⁻¹. Upon cooling, the β form does not transition back. (d) CPOM images of a single crystal of ditBu LT form (blue birefringence). The LT form rapidly transitions to the HT form (brown birefringence) upon heating in approximately 1.25 s. The average propagation speed of the phase boundary line is calculated to be 176 μm s⁻¹. Upon cooling, the HT form reversibly transitions to the LT form in 0.38 s, and the propagation speed is 579 μm s⁻¹.

address this molecular-level question to better understand cooperative transition in organic systems.

Cooperative polymorphic transitions are particularly fascinating. Resembling metal alloys, ²⁶ cooperative transitions in molecular crystals triggered by mechanical and/or thermal energy lead to intriguing properties such as the shape memory effect, ^{24,27–30} thermosalient effect, ^{27,31,32} and superelasticity. ³³ The ability of cooperative transition to convert microscopic molecular motion to macroscopic mechanical work has already gathered interest for molecular devices. ^{34–36} On the other hand, cooperative polymorphic transitions remain significantly understudied given their rare occurrence in molecular crystals. Reports on the molecular mechanisms underlying cooperative transitions are even more scarce.

In the field of organic electronics, there had not been a single report of cooperative polymorphic transition until our recent discovery in ditert-butyl [1]benzothieno[3,2-b]benzothiophene (ditBu-BTBT) and 6,13-bis-(triisopropylsilylethynyl)pentacene (TIPS-pentacene) single crystals. A major advantage of utilizing cooperativity in organic electronics is that such a transition mechanism preserves structural integrity and allows rapid reversible modulation of electronic properties. We hypothesized that the bulky side-chain rotation triggers this rare transition. With a better understanding of the molecular origin of cooperative transition, we can formulate molecular design rules to trigger cooperativity for future applications in organic electronics and molecular devices. We also emphasize the importance of the dynamics of side-chains beyond phase transitions of molecular

crystals, as previous works have shown that slight modulation of side-chains can lead to drastic differences in various properties, such as molecular packing and mechanical properties. 38,39

In this work, we further investigate the hypothesis that sidechain rotation is a molecular design rule for cooperative transition and demonstrate that the polymorphic transition mechanism is sensitive to even a single atom substitution. From ditBu-BTBT that exhibits a cooperative transition, we substitute a single atom in the side-chain from carbon to silicon. In the new system, bis(trimethylsilyl) BTBT (diTMS-BTBT), the bulkier silicon atom, alters the side-chain environment to inhibit side-chain rotation, thereby converting the original cooperative transition mechanism to one of nucleation and growth. As a result, we have access to two polymorphic transition pathways by a single atom substitution. By comparing the molecular environment between the two systems, we can pinpoint the molecular origin of each transition mechanism. We also demonstrate that both transition pathways have respective advantages for organic electronics that can be selectively accessed by this simple molecular design rule.

■ RESULTS AND DISCUSSION

Two Transition Pathways of Nucleation and Growth versus Cooperative Transition in Organic Electronics. To investigate the polymorphic transition pathways of diTMS-BTBT (abbreviated as diTMS) and ditBu-BTBT (abbreviated as ditBu), we first employed powder differential scanning

calorimetry (DSC) as a means to discover polymorphs. We note that the melting points of diTMS and ditBu have been reported in a previous work⁴⁰ as 215.3 and 277.1 °C, respectively. The DSC results indicated a reversible solid-state transition near 151 °C (Figure 1a) and 71 °C (Figure 1b) upon heating for diTMS and ditBu, respectively. With the change of a single atom from carbon to silicon, the transition temperature significantly increased, but both systems showed an enantiotropic relationship between polymorphs with similar enthalpy values, suggesting a larger entropic change for diTMS upon transition. We note that the ditBu single crystals studied previously^{24,37} agreed well with the DSC results, showing reversible low-temperature (LT) and high-temperature (HT) polymorphs. Thus, we next studied the polymorphic transition behavior of diTMS in their single-crystal forms.

Single crystals of diTMS were formed by drop-casting and by slow evaporation from various solvents. The key to dropcasting was using supersaturated solution in a high boiling point solvent so that the bulk crystallization outcompetes the coffee ring effect⁴¹ (see details in the Materials and Methods section). Drop-casted diTMS crystals were observed under a cross-polarized optical microscope equipped with a Linkam stage. Two crystal types were observed, denoted as α and β crystals, with characteristic angles 74° and 58° in the crystal habits, respectively. They formed concomitantly during dropcasting (Figure S1) or separately by controlling the solvent and concentration (Table S1). During annealing under a crosspolarized optical microscope, the α crystals showed polymorphic transitions (Figure 1c and Movie S1), while the β crystals sublimed without transition (Movie S2). These differences in transition behaviors also indicated that they were two different polymorphs. From the phonon region of the Raman spectra, 42,43 we were able to identify that the α crystal transitions into the β crystal (Figure S2). Variable-temperature Raman spectra of the diTMS α -to- β transition are shown in Figure S3.

On average, 10 pristine α crystals transitioned at 148.5 \pm 3.4 °C upon heating, similar to the DSC results. We note that there was a wide variation in the transition temperature depending on the quality of the crystals, which will be discussed later. However, the transformed diTMS single crystals did not show any signs of polymorphic transition upon cooling, indicating an irreversible transition that seems to contradict the DSC results. We believe that upon heating, the α form transitions to the β form because of stability switching from α to β after crossing the transition temperature; when cooled to below the transition temperature, β became metastable but cannot convert back to the stable α form possibly because of a high kinetic barrier to nucleation. In the powder form used in the DSC study, the kinetic barrier of β -to- α transition may be lowered because of a much higher density of defects and grain boundaries in powders.

The α -to- β transition in diTMS showed a single nucleation location, widespread growth directions of the new polymorph, and a slow irreversible transition that lasts several minutes (Figure 1c). These characteristics were in stark contrast to the ditBu crystal that showed a phase boundary line formation, directional propagation of the new polymorph, and a rapid reversible transition that spans seconds (Figure 1d, Movie S3). The average growth speed in the diTMS sample was 1.8 μ m s⁻¹, while the average propagation speed in ditBu was 176 μ m s⁻¹ upon heating and 579 μ m s⁻¹ upon cooling, more than 2 orders of magnitude faster. Similarly, Panda, Naumov, and

colleagues reported a drastic difference in propagation speed between two different transition mechanisms in (phenylazophenyl)palladium hexafluoroacetylacetonate crystals. ³² In this case, the growth speed in a nucleation and growth case (γ to β form) was ca. 43.4 μ m s⁻¹, and in the thermosalient transition case (α to γ form), which is analogous to cooperative transition described here, the speed was ca. 0.54 m s⁻¹, representing 4 orders of magnitude increase.

All diTMS single crystals exhibited a single-crystal-to-polycrystal transition behavior evident from the differently birefringent domains from cross-polarized optical microscopy (CPOM) (Figure S4, Movie S4), whereas ditBu single crystals showed single-crystal-to-single-crystal transition. We attribute the loss of single crystalline nature of diTMS after transition to the large structural differences between the parent and daughter forms, known to occur in the nucleation and growth^{20,22} mechanism. In contrast, the ditBu crystal can preserve structural integrity for multiple thermal cycles²⁴ of cooperative transitions because the structural differences between the polymorphs are very small. We believe the higher free energy barrier between the polymorphs in diTMS, characteristic of nucleation and growth, prevented reversibility, whereas the low free energy barrier between ditBu polymorphs, characteristic of cooperative transition, allowed rapid reversi-

In addition, creating surface defects on the diTMS crystals with syringe needles triggered nucleation from those locations and lowered the transition temperature, validating the nucleation behavior 20,21,37 (Figure S5, Movie S5). From a sample of 10 α single crystals each, pristine samples exhibited an average transition temperature of 148.5 \pm 3.4 $^{\circ}\mathrm{C}$ and defective samples 129 \pm 9.2 $^{\circ}\mathrm{C}$. Lowered transition temperature in defective crystals indicates that as nucleation initiates from the defects more easily, the free energy barrier to nucleation is lowered compared to that of the pristine crystals. All of these lines of evidence indicate that diTMS exhibits a nucleation and growth transition. We have validated the cooperative nature of the ditBu transition previously through introducing defects. 37

Surprisingly, this drastic change in polymorphic transition pathway results from a single atom substitution in the side-chains from silicon to carbon, with identical conjugated cores. This serves as an ideal platform to investigate the impact of subtle change of side-chain on the polymorphic transition pathway. We will first compare the structural characteristics before and after transition for diTMS and ditBu. Then, we will pinpoint the exact molecular origin of how a single atom substitution on the side-chain can alter the polymorphic transition pathway.

Characterization of Structural Changes during Polymorphic Transitions. To investigate the structure of both polymorphs of diTMS, larger crystals were grown from slow evaporation for single-crystal X-ray diffraction (SCXRD). Similar to drop-casted crystals, both polymorphs could be obtained by various experimental conditions. The β crystal was obtained from various organic solvents such as toluene, acetone, and chloroform, and the α crystal was obtained from tetralin (Table S1).

From the structures obtained from SCXRD at room temperature, α form is triclinic with a $P\overline{1}$ space group, and β form is monoclinic with a $P2_1/c$ space group. From α to β form, a slight increase in the core tilt angle from 42.1 to 47.8° leads to an increased core overlap in the β form, and the

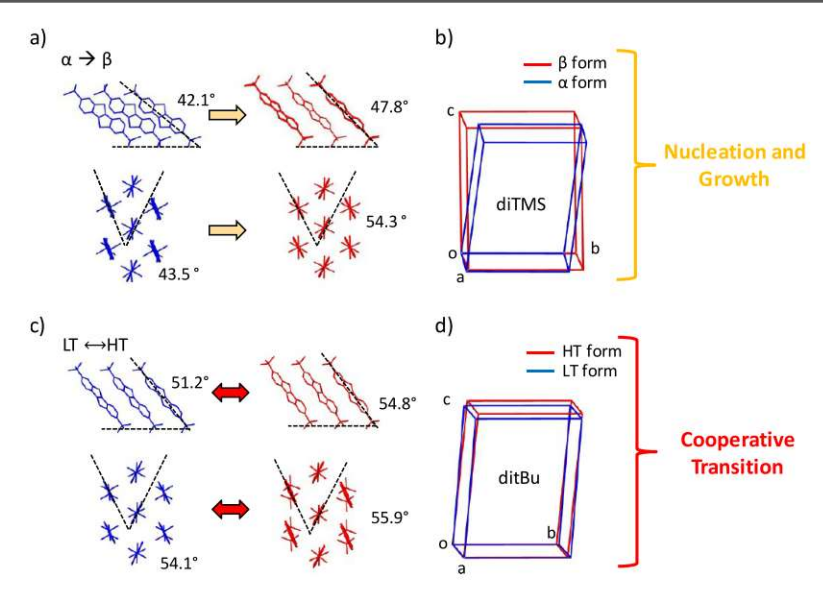


Figure 2. Molecular structural differences between nucleation and growth and cooperative transition. (a) α (blue) and β (red) polymorph structures of diTMS showing the core tilt and herringbone angle. Both forms were collected at 25 °C. Hydrogen atoms are omitted for better visualization. (b) Unit cell overlap of α and β diTMS polymorphs. The diTMS system shows a nucleation and growth mechanism. (c) Core tilt angle and herringbone angle of LT (blue) and HT (red) structures of ditBu. (d) Unit cell overlap of LT and HT ditBu polymorphs. The ditBu system shows a cooperative transition mechanism.

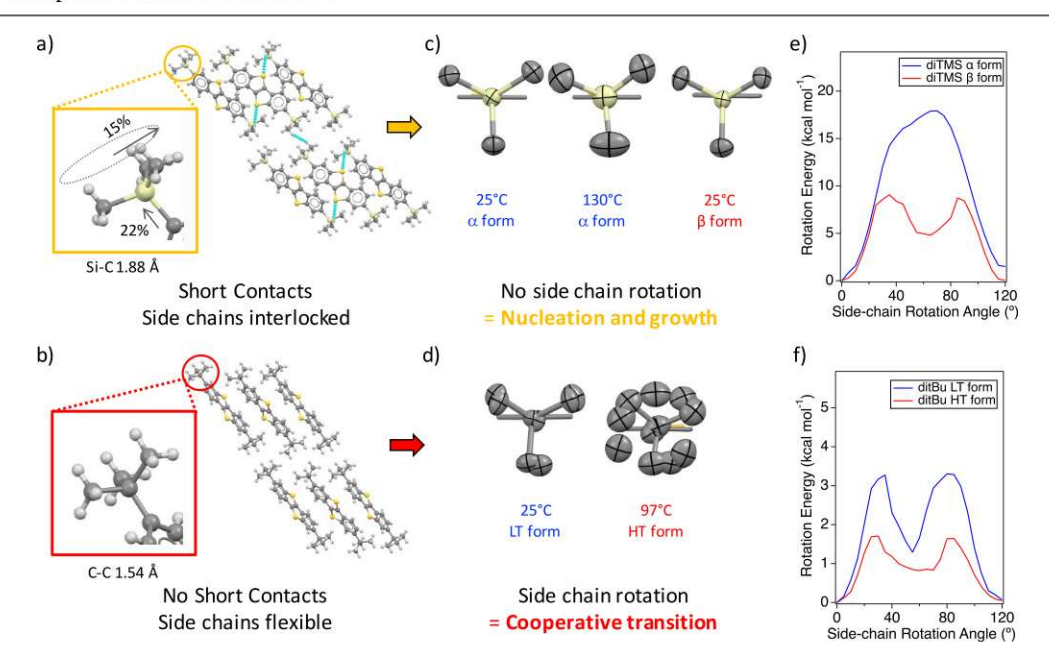


Figure 3. Side-chain environment differences between nucleation and growth and cooperative transition. (a) Two layers of molecules from the diTMS α form at 25 °C displaying short contacts (in cyan). As a result, side-chains are more interlocked. Two major short-contacts exist from the side-chain, which are both intralayer and interlayer. The inset highlights the 22% increase in bond length and 15% increase in side-chain radius from the single atom substitution. The silicon—carbon bond length is measured as 1.88 Å. (b) Two layers of molecules from the ditBu LT form at 25 °C displaying the absence of short contacts. As a result, side-chains have more room. The inset highlights the less bulky tBu side-chains. The carbon—carbon bond length is measured as 1.54 Å. (c) Ellipsoid representation of side-chains in diTMS from structures at 25 and 130 °C of the α form and at 25 °C of the β form. Even at an extremely HT of 130 °C, only relatively small thermal vibrations are evident in the diTMS side-chains, showing no signs of rotation. (d) Ellipsoid representation of side-chains in ditBu from structures at 25 °C of the LT form and at 97 °C of the HT form. Compared to the diTMS side-chains, some disorder is seen even at room temperature, which extends to full rotation after transition to the HT form. (e) DFT simulations of the energy barrier of rotation for the ditBu LT form and HT form. As predicted from structural data, the more interlocked side-chain environment of diTMS shows a much higher energy barrier compared to the more flexible environment of ditBu.

herringbone angle significantly increases from 43.5 to 54.3° after transition (Figure 2a). For unit cell lengths, there is approximately 16% decrease in the *a*-axis and a 12 and 5%

increase in the b- and c-axis, respectively (Table S2). For the unit cell volume, there is an approximately 1% increase from α to β form. Corroborating that nucleation and growth follows a

reconstructive transition mechanism, we observe a change in the symmetry and large changes in the unit cell (Figure 2b). In contrast, cooperative transition from the LT to the HT form in ditBu does not change the symmetry of the system, both monoclinic with a $P2_1/c$ space group. For the ditBu system, the LT crystal structure is obtained at room temperature, but the HT form can only be obtained from HT at 97 °C. The core tilt angle slightly increases from 51.2 to 54.8°, and the herringbone angle increases from 54.1 to 55.9°. For the unit cell, lengths of the a- and c-axis increase approximately 3%, while the b-axis decreases about 2%. The unit cell volume increases approximately 3.7% from the LT form to the HT form, mainly due to the thermal expansion from room temperature to 97 °C. As seen from the unit cell comparison in Figure 2b,d, the change in the unit cells of ditBu polymorphs is very small compared to those of diTMS, consistent with the displacive, cooperative nature of the transition.

From the process of obtaining single-crystal structures, the distinct advantages of both transition pathways were evident. A major advantage of nucleation and growth is that both α and β forms are accessible at ambient conditions by changing experimental conditions, so each polymorph can be separately used for SCXRD experiments. Because nucleation and growth systems have a relatively high transition barrier, it follows that when the metastable form is kinetically accessed, it remains stable, as in the case of the diTMS β form. For a cooperative transition, the minimal change in the structure of the polymorphs allows preservation of structural integrity before and after the transition. This is significant as a single ditBu crystal can be used to collect both the LT and HT forms from variable-temperature SCXRD.

By comparing the molecular environments of diTMS and ditBu before transition, we can investigate the molecular origin of the two transition pathways. Importantly, we can pinpoint the difference in transition pathway to the change in the side-chain environment. For instance, the core tilt angle with the heavier silicon atom in diTMS is 42.1°, while with carbon in ditBu it is 51.2°. This major change in tilt angle causes the bulkier diTMS side-chains to have much closer interactions with the core as we will discuss later. Because the rotation of the ditBu side-chains is the driving force for cooperative transition,²⁴ we will investigate if these major differences in the side-chain environment impact its rotation and help us understand the molecular origin of the two polymorphic transition pathways.

Molecular Origin of Nucleation and Growth versus Cooperative Transition. From our crystal structures of diTMS α form and ditBu LT form, we can pinpoint the molecular changes resulting from the single atom substitution in the bulky side-chain. Using the Mercury software 44 (v.3.9), the silicon-carbon bond of diTMS was measured as 1.88 Å, which represents ca. 22% increase from the carbon-carbon bond of ditBu (1.54 Å). The bulkiness of the side-chains was measured by the side-chain radius, which we define as the distance from the central side-chain atom to the farthest hydrogen atom. The TMS side-chain radius was measured as 2.39 Å and the tBu side-chain radius as 2.08 Å. Thus, in diTMS, we see a ca. 15% increase in the side-chain radius compared to that in ditBu (Figure 3a,b inset). Although this single atom substitution only causes angstrom-level changes in the molecule, the consequences become macroscopic, impacting the entire packing environment of diTMS. In particular, although the two systems showed the same layered,

herringbone packing, there were significant changes to their core tilt angle $(51.2^{\circ} \text{ to } 42.1^{\circ})$ and herringbone angle $(54.1^{\circ} \text{ to } 43.5^{\circ})$, as shown earlier in Figure 2a,c. The smaller core tilt angle and herringbone angle in diTMS indicate that the sidechains lean closer to the core of the neighboring molecule (Figure 3a).

The stark difference in packing environment between the two systems is manifested in their intermolecular short-contact interactions. Short-contacts exist in neighboring molecules if the measured distance between two neighboring atoms is smaller than the sum of the van der Waals radii of the atoms. 45 We note that we adopted a definition of short-contacts (given directly by Mercury 3.9) that is slightly different from the recent report by Purdum, Loo, and colleagues, 46 in that we explicitly considered hydrogen-hydrogen interactions in our analysis. The α form of diTMS contains two short-contact interactions: one intralayer and another interlayer (Figure 3a). Both short-contacts involve the hydrogen atom of the sidechain: one intralayer with the thiophene sulfur atom of the core and another interlayer with the neighboring side-chain hydrogen atom. On the other hand, in the LT form of ditBu, no short-contacts exist (Figure 3b). This indicates that compared to the diTMS side-chains, the ditBu side chains have more room. We thus infer that a single atom substitution from carbon to silicon leads to a tighter packing environment that restricts the movement of the diTMS side-chains, while there is ample room for the ditBu side-chains to move and rotate.

To confirm this hypothesis, we utilized synchrotron SCXRD to visualize the side chains of the α and β forms of diTMS and LT and HT forms of ditBu. As expected, the interlocked diTMS side-chains remain static at both 25 and 130 °C before transition in the α form and at 25 °C after transition in the β form (Figure 3c). In fact, even at a significantly higher temperature of 130 °C, the diTMS side-chains were static without much dynamic disorder. In comparison, the ditBu side-chains show partial dynamic disorder even at 25 °C and show full rotational motion at 97 °C in the HT form (Figure 3d). These SCXRD results clearly indicate that a single atom substitution of the side-chain caused significant changes to the packing environment that restricts the full rotational motion of the side-chains for diTMS.

In addition, the stark contrast in side-chain behavior was confirmed by monitoring the full width at half maximum (fwhm) of the side-chain peaks from in situ Raman spectroscopy of the two systems (Figure S6). An increase in fwhm of a peak corresponds to an increase in disorder for that specific vibration. For ditBu, a clear, abrupt increase in fwhm of the side-chain C–H stretching peak was observed upon transition, while in diTMS, no abrupt change in fwhm was consistently observed besides the gradual peak broadening upon temperature increase. This confirms that the diTMS side-chains remain static before and after the transition.

To further confirm the important role of side-chains in determining the transition pathway, we conducted plane wave density functional theory (DFT) simulations to calculate the rotational energy barrier associated with the polymorphs in the two systems (see details in the Materials and Methods section). We directly incorporated SCXRD structures, and for ditBu LT and HT forms, the disorders were eliminated for the calculations. We created a test set of distinctly different initial configurations that were obtained by rotating one side-chain in a crystal in 5° increments until a full rotation of 120°

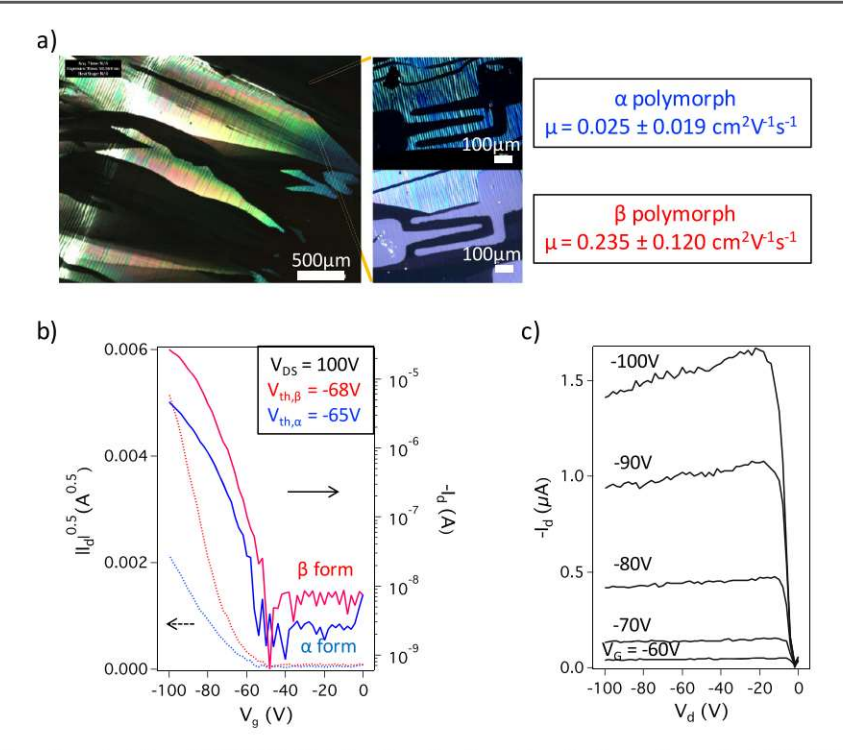


Figure 4. Thin-film transistor characteristics of diTMS highlighting the advantage of nucleation and growth. (a) (Left) POM image of a thin film containing both α and β forms of diTMS from blade-coating. The bright regions are the α form and the dark regions are the β form. (Right) POM images of thin-film transistors of α and β forms and their apparent charge carrier mobility. (b) Transfer curves of α (blue) and β (red) thin-film transistors. The dashed lines correspond to the y-axis on the left, and the solid lines correspond to the y-axis on the right. Values for the drain voltage and threshold voltages are given in the inset. (c) Output curve of the β thin-film transistor. Gate voltages are measured from -60 to -100 V.

was made (threefold symmetry). Each of these initial configurations was then run in a geometry-optimized DFT simulation (using Quantum ESPRESSO) such that the side-chain atoms under consideration remained fixed at their initial position, while the rest of the atoms were allowed to relax around this rotational displacement. This was done to make sure that there were no artifacts related to van der Waals repulsion. Each of these simulations resulted in a calculation of a characteristic energy value associated with a particular angle of rotation induced in the system. The results for both polymorphs of diTMS and ditBu are shown in Figure 3e,f.

For diTMS, the rotation energy was much larger for the α form, in which the maximum was ca. 17.9 kcal mol⁻¹, than for the β form, ca. 9.1 kcal mol⁻¹ (Figure 3e). We observe that the rotation energy decreases in the β form after a large change in structure via nucleation and growth. For ditBu, the rotation energy for the LT form is ca. 3.3 kcal mol⁻¹, while for the HT form, it is ca. 1.7 kcal mol⁻¹ (Figure 3f). The decrease in rotation energy at the HT form agrees with our SCXRD data that display fully disordered rotating ditBu side chains at the HT form. After a cooperative transition occurs, the molecular environment favors side-chain rotation, hence lowering the rotational energy barrier for ditBu side-chains. Comparing the diTMS with the ditBu system before transition, the rotation energy of the α form of diTMS (ca. 17.9 kcal mol⁻¹) is more than a factor of 5 higher than that of the LT form of ditBu (ca. 3.3 kcal mol⁻¹), confirming our observation that the diTMS side-chains are more interlocked compared to the ditBu side chains. After transition, the rotation energy of the β form of diTMS (ca. 9.1 kcal mol⁻¹) is also higher than that of the HT form of ditBu (ca. 1.7 kcal mol⁻¹), indicating that the diTMS

side-chains remain static after nucleation and growth, while the ditBu side-chains become disordered after cooperative transition.

A single atom substitution of the ditBu bulky side chain leads to stronger intra- and interlayer interactions and thus more restricted packing environment of the diTMS system that constrains the rotation of the side-chains. This mechanistic analysis confirms our hypothesis that the rotation of the tBu side chains drives cooperative transition, whereas hindering the rotation of TMS side-chains leads to nucleation and growth. Therefore, promoting the rotation of side-chains can be used as a molecular design rule to access the rarely observed cooperative transition. Modifying the side-chain can also serve as a useful tool to access both polymorphic transition pathways.

Impact of Two Transition Pathways on Organic Electronic Devices: Nucleation and Growth. We demonstrate the respective advantages of nucleation and growth and cooperative transition in organic electronic devices. The nucleation and growth mechanism allows easy access to different polymorphs at ambient conditions, possibly owing to higher nucleation barriers to polymorphic transitions that engender the high kinetic stability of polymorphs. On the other hand, the cooperative transition mechanism allows rapid and reversible interconversion between polymorphs and electronic states, thanks to molecular cooperativity and a lower transition barrier.

We first demonstrate applications of the nucleation and growth mechanism to access diTMS polymorphs for studying the crystal structure—charge transport relationship. Because in single crystals, α and β forms of diTMS were easily accessed by

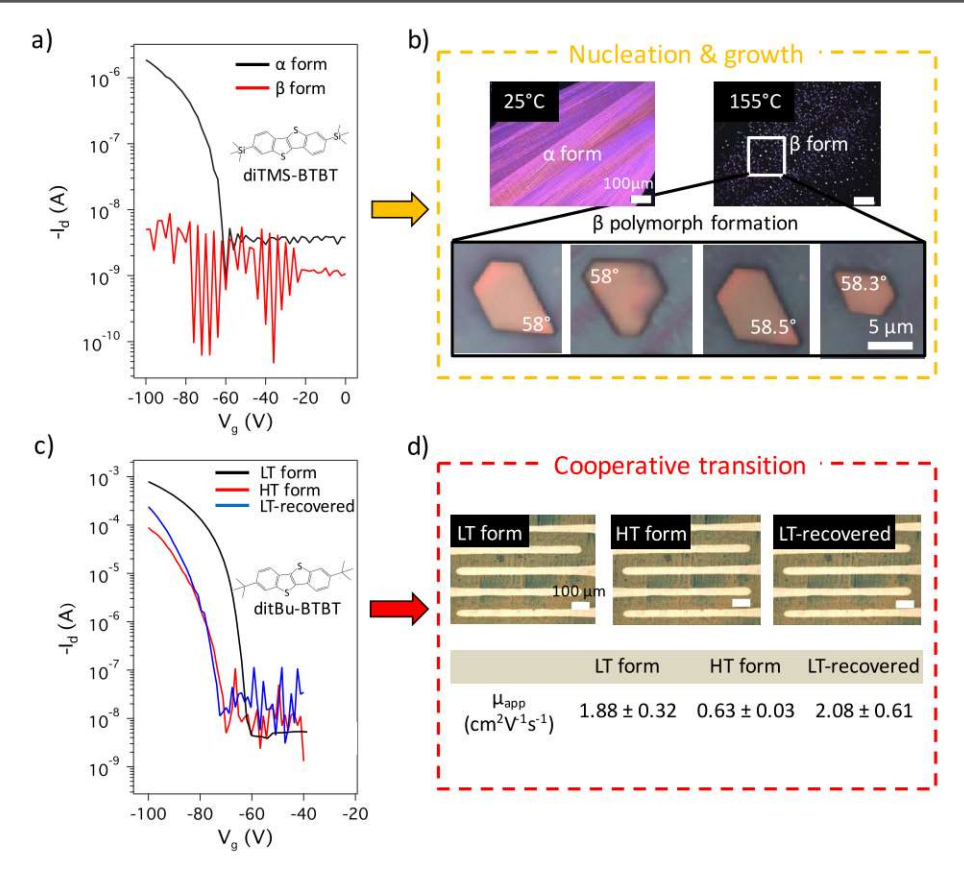


Figure 5. Application of both polymorphic transition pathways to diTMs and ditBu thin-film transistors. (a) Transfer curves of the diTMS thin film in the α form (black) and, after transition, in the β form (red). After transition, there is no charge transport in the β device. (b) POM images of the α form before transition at 25 °C and after transition at 155 °C to β form. The transformed crystals display the characteristic angle for the β form. (c) Transfer curves of the ditBu thin film in the LT form (black), in the HT form (red) after thermally induced transition, and after cooling back to the LT form (blue). (d) OM images of the LT form, HT form, and LT form recovered at 25 °C.

using different solvents, we screened various solvents to capture both polymorphs in diTMS thin films from meniscusguided blade-coating. As Chloroform, tetralin, and chlorobenzene were used to fabricate thin films suitable for field-effect transistors (Table S3). When blade-coating with chloroform (Figure 4a) or tetralin (Figure S7), extremely high and low birefringent regions coexisted on a single substrate. Using XRD and Raman spectroscopy, the dark region was confirmed as the β form and the bright region was confirmed as the α form (Figures S8 and S9). When we used other solvents, such as dichlorobenzene and chlorobenzene, we obtained low birefringent films, yielding the β form. We note that for the ditBu system that exhibits a cooperative transition, we could access only the LT form at room temperature but not the HT form; the HT form could be obtained only by heating.

We fabricated top-contact bottom-gate thin-film transistors (see the Materials and Methods section) on both α and β regions of diTMS thin films. We used silicon substrates with spin-coated polystyrene (PS, 290k MW) as the dielectric layer for best performance (capacitance measured using quasi-static capacitance voltage measurement to be 8.8 nF cm⁻², Keysight). We note that the PS dielectric layer produced a slightly different morphology upon blade-coating (Figure S10), but the electronic performance was more stable compared to using a SiO₂ dielectric layer. The transfer curves of both α and β forms are shown in Figure 4b. For the stable α form at room temperature, the saturation regime mobility (VDS = -100 V)

at room temperature over 10 devices was 0.025 \pm 0.019 and for the metastable β form was 0.235 \pm 0.120 cm² V⁻¹ s⁻¹. The output curve of a β film is shown in Figure 4c. The α film channel region morphology, output curve, and α and β gate-dependent mobility are given in Figure S11. The α film always produced lower electronic performance compared to the β film. In addition to the possible impact from film morphology and additional grain boundaries, the order of magnitude higher performance of β devices may be related to a less tilted conjugated core in the β form (Figure 2a), resulting in more π - π core overlap that contributes to higher charge carrier mobility.

Impact of Two Transition Pathways on Organic Electronics: Cooperative Transition. We next demonstrate applications of cooperative transitions for reversible switching of electronic properties in comparison to that of the nucleation and growth mechanism. To do so, we measured the charge carrier mobility before and after thermally triggering the transitions in thin films of both systems. For diTMS thin films, similar to the α -to- β transition in single crystals, we observed a nucleation and growth mechanism (Figure S12) on bladecoated (Movies S6 and S7) and spin-coated (Movie S8) samples. We confirmed the α -to- β transition using Raman spectroscopy (Figure S13) and synchrotron grazing incidence wide-angle X-ray diffraction (GIXD) (Figure S14).

We thermally triggered nucleation and growth on α thin-film transistors of diTMS, and their transfer curves are shown

before and after the transition (Figure 5a). As the α thin film was heated up to the transition temperature of 155 °C, it formed small β crystals with their characteristic angle of 58° (Figure 5b). As expected, the reconstructive transition destroys the device after transition, and no charge transport was detected.

On the other hand, cooperative transition opens new opportunities for application in organic electronics. The cooperative nature of the transition with minimal changes in the unit cell results in rapid reversible switching with no damage to devices. The electronic performance was measured for the LT form at room temperature, the HT form at 90 °C, and the recovered LT form back at 40 °C (Figure 5c). Measured over four devices, the apparent mobilities were, on average, 1.88 ± 0.32 , 0.63 ± 0.03 , and 2.08 ± 0.61 cm² V⁻¹ s⁻¹, respectively. The CPOM images of devices show no visible change of the thin film after transition (Figure 5d). Full transfer curves, output curve, and gate voltage-dependent mobility are given in Figure S15. The difference in mobility is significant, which is more than 3 times higher in the LT form compared to that in the HT form. Furthermore, the preservation of structural integrity from cooperative transition allows rapid reversible switching between the two polymorphs for multiple cycles. Even after five thermal cycles, the charge mobility recovers close to its initial performance²⁴ (Figure S16).

By tailoring the bulkiness of the side-chain with a single atom substitution, we successfully altered the type of polymorphic transition from conventional nucleation and growth to cooperative transition and investigated their impact on electronic performance. Nucleation and growth is favorable for a fundamental structure—property study of the polymorphs. However, triggering the transition in situ destroys the thin film of diTMS. On the other hand, cooperative transition occurs rapidly without altering the thin-film morphology of ditBu, opening opportunities for designing next-generation electronics capable of dynamic modulation of electronic properties.

In summary, we investigated and compared the molecular mechanism of two distinct polymorphic transition pathways through a single atom substitution in bulky side-chains of BTBT-based organic semiconductors. Substituting the carbon atom in the side-chains of ditBu-BTBT with a bulkier silicon atom produced a significant 22% increase in the bond lengths of diTMS-BTBT that consequently impacted the molecular packing environment, restricting side-chain rotation. This change was manifested in the creation of two pairs of shortcontacts associated with the side-chains in diTMS-BTBT, in contrast to the absence of short-contact interactions in ditBu-BTBT. By SCXRD and Raman spectroscopy, we confirmed the side-chain rotational motion in ditBu and the inhibited motion in the diTMS side-chains after transition. From DFT calculations, we simulated the energy barriers for side-chain rotation in the two systems to quantify the drastic difference in the side-chain packing environment. Before transition, the rotation energy was ca. 17.9 kcal mol⁻¹ for the diTMS α form side-chain, compared to a much lower ca. 3.3 kcal mol⁻¹ for the ditBu LT form side-chain. After transition, the rotation energy was ca. 9.1 kcal mol⁻¹ for the diTMS β side-chain and ca. 1.7 kcal mol⁻¹ for the ditBu HT side-chain. These results confirmed that the significant change in the packing environment resulting from a substitution from carbon to silicon hindered the rotation of diTMS side-chains.

We then investigated the advantages of both polymorphic transition pathways on organic electronic devices. Nucleation and growth allows kinetic access to both forms of polymorphs in diTMS thin films, which can be fabricated concomitantly on a single substrate. This presents an ideal platform for structure—electronic property studies. Cooperative transition allows rapid reversible in situ access to different polymorphs on the same device and preserves structural integrity for multiple transition cycles because of minimum changes in the polymorphs. This enables opportunities for next-generation multifunctional organic electronics.

This work demonstrates that polymorphic transition pathways are extremely sensitive to subtle changes in molecular structures and that side-chain rotation is a molecular design rule to modulate the polymorphic transition mechanism. Our work suggests the importance of molecular movements in phase transformations of molecular crystals beyond the field of organic electronics. In our case, the weak molecular interactions were altered just enough to allow rotation of the side chains in the ditBu system and inhibit rotation in the diTMS system. By promoting or inhibiting bulky side-chain rotation, we can selectively access both polymorphic transition pathways of cooperative transition and nucleation and growth. We confirm our hypothesis that bulky side-chain rotation triggers cooperative transition and also presents a novel approach to apply the advantages of two different transition pathways in organic electronic devices.

MATERIALS AND METHODS

Materials Synthesis. Details of the synthesis steps for both ditBu-BTBT (ditBu) and diTMS-BTBT (diTMS) are published in a previous work. 1

Single-Crystal Sample Preparation. Details of fabricating single crystals of ditBu are included in previous work. For diTMS samples used for in situ microscopy, a stock solution of tetralin in concentrations ranging from 6 to 11 mg mL⁻¹ was mainly used for drop-casting. Up to 2–5 μ L of solution was drop-cast directly onto silicon substrates or to nine-well glass plates for slow evaporation overnight. α crystals usually formed at higher concentration solutions (~10 mg mL⁻¹) and β crystals at lower concentration (~6 mg mL⁻¹). For fabricating larger single crystals of diTMS for SCXRD, α crystals could only be obtained by seed crystallization of the previous drop-casted α crystal in ethyl acetate (2 mg mL⁻¹) for slow evaporation. β crystals were obtained from slow evaporation in toluene (5 mg mL⁻¹), acetone (1 mg mL⁻¹), or chloroform (5 mg mL⁻¹). Table S1 summarizes all conditions for fabricating diTMS single-crystal polymorphs.

Thin-Film Sample Preparation. The diTMS thin films for in situ microscopy and in situ GIXD were fabricated via meniscus-guided coating (Table S2). The α films, which are distinguishable under a cross-polarized optical microscope as "bright" regions, were formed from either chloroform (5 mg mL-1) at a blade speed of 0.3 mm s-1 at room temperature or tetralin (6 mg mL $^{-1}$) at 0.3 mm s $^{-1}$ at 100 $^{\circ}$ C or 0.5 mm s⁻¹ at 150 °C. Note that the formation of α films was stochastic. The β films were the darker regions in the mentioned α film conditions and were formed in dichlorobenzene (10 mg mL⁻¹) at various speeds (0.1-5 mm s⁻¹) at 100 °C and chlorobenzene (10 mg mL⁻¹) at various speeds (0.1-5 mm s⁻¹) at 100 °C. The diTMS thin films for GIXD were fabricated via spin-coating from chloroform (2 mg mL⁻¹) with a capping layer to prevent sublimation. The same capping layer was used as the one previously reported,4 a 15 wt % aqueous solution of polyvinylpyrrolidone (MW 40k). The capping layer was prepared by stirring overnight, followed by filtration using the 0.45 μ m poly(vinylidene difluoride) syringe filter. The solution was then spin-coated on top of the diTMS thin film at a speed of 4000 rpm and baked at 100° for 30 min.

Cross-Polarized Optical Microscopy. Single-crystal or thin-film samples of diTMS were placed in a heating chamber with Linksys32 temperature control under a Nikon H550S with a high-speed camera (infinity 1). The heating chamber was capped with a sealable lid during heating and cooling cycles, and the rate was kept constant at 5 °C min⁻¹. Time-lapse images were taken for all in situ experiments with various frame rates ranging from 5 to 10 fps. Image analysis was performed with softwares Nikon NIS Elements, Linksys32 data capture, and ImageJ.

Single-Crystal X-ray Diffraction. The single-crystal structures for the ditBu LT form at 25 °C and the HT form at 97 °C and the diTMS β form at 25 °C were collected at the G.L. Clark X-ray facility at the University of Illinois at Urbana-Champaign. Diffraction data were collected on a Bruker D8 Venture equipped with a four-circle kappa diffractometer and a PHOTON 100 detector. The Iµs microfocus Mo (λ = 0.71073 Å) source supplied the multimirror monochromated incident beam. The sample was mounted on a 0.3 mm loop with a minimal amount of Paratone-N oil. Data were collected as a series of φ and ω scans at the corresponding temperatures for the two systems. Data were integrated and filtered for statistical outliers using SAINT (Bruker, 2014) and then corrected for absorption by integration using SADABS v2014/4 (Bruker, 2014). The structure was phased by direct methods and refined using the software package SHELX-2014-3 (Sheldrick, 2008). The single-crystal structures for the ditBu LT form at 25 °C and the HT form at 97 °C has been previously reported² with cif files registered with the Cambridge Crystallographic Data Center (CCDC) as CCDC 1570908 (ditBu LT form at 25 °C), 1570909 (ditBu HT form at 97 °C).

The single-crystal structures for the diTMS α form at 25 and 130 °C and the β form at 25 °C were collected at NSF's ChemMatCARS (Sector 15) of the Advanced Photon Source, Argonne National Laboratory. The clear hexagonal plate crystals were mounted on a 5 μ m diameter glass fiber tip with epoxy and heated up to 130 °C with an open-stream Leister heater. The beam energy was 30 keV (0.41328 Å), and the beam size at the sample was $0.15 \times 0.15 \text{ mm}^2$. Data were collected using a Huber 3 circles diffractometer with a kappa angle offset of 60° and equipped with a Pilatus3X 1M (CdTe) detector. The distance between the detector and the crystal was 130 mm. A total of 720 frames were collected at two θ -angles sitting at 0° and ω -angles sitting at -180°, followed by two different kappa = 0° and kappa = 15°, respectively. The data were collected with the φ -angle scanned over the range of 360° using shutterless mode. A user-friendly data collection software was used. Tiff frames were converted to Bruker sfrm format. Data integration was performed with the APEX II suite software. The reduction of data was conducted with SAINT v.8.32B and SADABS v.2013 programs included in the APEX suite. The structure solution and refinement were carried out with the SHELX software using the XPREP utility for the space group determination and the XT and XL programs for the structure solution and refinement, respectively.

Raman Spectroscopy. Raman spectra were recorded from single crystals and thin films grown on Si substrates, and they were the same samples made for in situ microscopy experiments. A Raman confocal imaging microscope with a 532 nm laser (Laser Quantum Ventus 532 with max power 50 mW) and 50× long working distance objective lens (HORIBA LabRAM HR 3D) equipped with HORIBA Synapse back-illuminated deep-depletion CCD camera was used to collect spectra. Using a 300 g mm⁻¹ grating, we used a scan exposure time of 10 s. An optical density filter of OD = 0.3 was used (OD = log(power transmission factor)), and no beam damage was observed on the sample. For variable-temperature experiments, the samples were collected using a Linkam THMS600 heating stage with a closed chamber. The heating and cooling rate was kept at 5 °C min⁻¹.

X-ray Diffraction. XRD data of diTMS single crystals and blade-coated thin films were taken to identify their polymorphs. Single crystals were placed firmly on copper tape, and thin-film samples (on silicon substrates) were taped to glass slides for the measurement using a Panalytical Phillips X'pert MRD diffractometer with a high-speed PIXcel line detector (pixel size 55 microns) with Cu $K\alpha$

radiation at a power of 45 mV and 40 mA and at a wavelength of 0.15418 nm. We used a point focus beam with a parallel-plate collimator with a flat graphite monochromator. Fast scans were performed with a step size of 0.05° and a step time of 0.5° , and detailed scans were performed using a step size of 0.05° and a step time of 2 s.

DFT Simulations. We conducted plane wave DFT simulations to obtain geometry-optimized structures and the corresponding energetics of the rotational barrier of the side-chains in diTMS and ditBu. All the simulations were performed using the Quantum ESPRESSO code. Our system consisted of a periodic unit cell lattice containing 96 atoms. Because of the intensive nature of the calculations involved for a system even of this size, simulating bigger system sizes was essentially out of reach even with access to a local supercomputer. Perhaps more importantly, because the rotation of the bulky side-chains will affect and be affected by, chiefly, its nearest neighbors, we expect that no significant changes in the energy barriers are likely to result if we increased the size of the unit cell, but we were unable to test this assumption. We used a cutoff energy of 60 Ry and a $2 \times 4 \times 2$ k-mesh for the LT and HT forms of ditBu and the α phase of diTMS, and we used a $4 \times 3 \times 2$ k-mesh for the β phase of diTMS to achieve a targeted convergence of below 0.005 eV in energy. The simulations were performed with norm-conserving Perdew-Zunger pseudopotentials within the local density approximation level of theory.

Grazing Incidence X-ray Diffraction. GIXD measurements were performed at beamline 8-ID-E of Advanced Photon Source at the Argonne National Laboratory. Data were collected with an incident beam energy at 7.35 keV on a two-dimensional (2D) detector (Pilatus 1M). WxDiff software was used to apply corrections for detector nonuniformity, beam polarization, and detector sensitivity and to reshape the 2D data into the representation q_z versus q_{xy} . The incident angle was set at 0.2° . Each of the peaks analyzed was fitted with a Gaussian function to obtain an accurate peak position. The measured peak positions were then used with a python-based algorithm to determine the crystal structure.

Thin-Film Transistor Fabrication and Characterization. We used a 10 mg mL⁻¹ solution of ditBu with 50 wt % PS in tetralin at a blade speed of 0.05 mm s $^{-1}$ at 95 $^{\circ}C$ and a 5 mg mL $^{-1}$ solution of diTMS with 50% PS (MW 290k, Sigma-Aldrich) in chloroform at a blade speed of 0.3 mm $\ensuremath{\text{s}^{-1}}$ at room temperature for meniscus-guided coating.³ The ditBu thin films were deposited on a trichloro(phenyl)silane-modified Si/SiO₂ substrate with dielectric SiO₂ of 300 nm thickness. The diTMS thin films were deposited onto a PS spincoated Si/SiO₂ substrate with dielectric SiO₂ of 300 nm thickness. Spin-coating was done at 2500 rpm with PS in dichlorobenzene (40 mg mL⁻¹) with annealing at 100 °C for 30 min afterward. For both ditBu and diTMS, the same top-contact bottom-gate architecture was used with MoO₃ (8 nm) and silver (35 nm) thermally evaporated (Kurt J. Lesker Nano 36) onto shadow-masked thin-film samples. The MoO₃ layer was inserted to facilitate charge injection and alleviate the high contact resistance, 1,6 reducing the threshold voltage. For ditBu devices, the channel length was 73 μ m and width 4380 μ m, while diTMS devices had a channel length of 40 μ m and a width of 800 μ m. Capacitance was measured for diTMS devices as 8.8 nF cm⁻² with a PS dielectric layer using the quasi-static capacitance voltage measurement method (Keysight Technologies). Electronic performance was measured in a nitrogen atmosphere using a Keysight B1500A semiconductor parameter analyzer. The field-effect mobility was calculated with standard equations for the saturation regime

$$\mu_{\text{sat}} = \left(\frac{\partial (I_{\text{ds}})^{0.5}}{\partial V_{\text{g}}}\right)^2 \frac{2L}{WC_{\text{i}}} \tag{1}$$

where L, W, and $C_{\rm i}$ are the channel length, channel width, and capacitance of the dielectric, respectively. $V_{\rm DS} = -100$ V was used for the saturation regime for all cases. HT measurements were conducted in the same semiconductor parameter analyzer with a temperature-controlled hot plate and a consistent heating and cooling rate of approximately 10 °C min⁻¹ in a nitrogen atmosphere. The ditBu

devices were measured at room temperature and 90 $^{\circ}$ C, and the diTMS devices were measured at room temperature and 155 $^{\circ}$ C. At higher temperatures, the samples were given 1 min of stabilization time before measurement.

ASSOCIATED CONTENT

Supporting Information

The Supporting Information is available free of charge on the ACS Publications website at DOI: 10.1021/acs.chemmater.9b03436.

Movie of nucleation and growth of the diTMS α crystal shown in Figure 1c; movie of sublimation of the diTMS β crystal with no transition; movie of cooperative transition of the ditBu LT crystal shown in Figure 1d; movie of nucleation and growth of another diTMS α crystal showing single-to-polycrystalline transition; movie of nucleation and growth of a needle-pricked diTMS α crystal shown in Figure S5; movie of nucleation and growth of a diTMS α thin film (bladecoating, chloroform); movie of nucleation and growth of a diTMS α thin film (blade-coating, tetralin); and movie of nucleation and growth of a diTMS α thin film (spincoating, chloroform) (ZIP)

Crystallographic data for the ditBu-BTBT LT form at 25 °C (CIF)

Crystallographic data for the ditBu-BTBT HT form at 97 °C (CIF)

Crystallographic data for the diTMS-BTBT α form at 25 °C (CIF)

Crystallographic data for the diTMS-BTBT β form at 27 °C (CIF)

 α and β polymorphs of diTMS single crystals formed concomitantly on the same substrate from drop-casting; phonon region Raman spectra of diTMS crystals displaying distinct characteristics between the α and β polymorphs; variable-temperature Raman spectra of diTMS α crystal transitioning to a β crystal; CPOM images of a single-to-polycrystalline transition in α -to- β transition in a diTMS single crystal; CPOM frames of nucleation and growth on needle-pricked crystals; comparison of side-chain behavior in diTMS and ditBu from variable-temperature Raman spectra; CPOM images of α and β thin films formed on the same substrate from meniscus-guided coating from tetralin solution; specular XRD on various blade-coated thin films to confirm polymorphidentification; Raman spectra on a blade-coated tetralin sample that contains both dark and bright regions; CPOM image of the thin-film morphology used for thin-film transistors without and with a PS dielectric layer; α thin-film transistor channel region morphology, output curve of a α thin-film transistor, and gate voltage-dependent apparent mobility on a α thin-film transistor and β thin-film transistor; CPOM images of an α -to- β transition in thin films blade-coated from tetralin; Raman spectroscopy characterization of the blade-coated tetralin film of α and β polymorphs; GIXD peaks of spin-coated samples at 25 °C and 206 °C; transfer curves for the LT, HT, and recovered LT forms of ditBu devices, output curve of a ditBu LT form thin-film transistor at room temperature, and gate-voltage dependent apparent mobility on ditBu thin-film transistor devices at the LT, HT, and recovered LT forms; apparent mobility measured in four ditBu

thin-film transistor devices over five thermal cycles at LT form, 40 °C (blue), and HT form, 90 °C (red); diTMS single-crystal fabrication conditions for in situ microscopy, Raman spectroscopy, and SCXRD; unit cell information for polymorphs of diTMS and ditBu; and diTMS thin-film fabrication conditions for accessing various polymorphs (PDF)

AUTHOR INFORMATION

Corresponding Author

*E-mail: yingdiao@illinois.edu.

ORCID ®

Nikita Sengar: 0000-0001-7549-2095 Yves H. Geerts: 0000-0002-2660-5767 Paulette Clancy: 0000-0002-0468-6420 Ying Diao: 0000-0002-8984-0051

Notes

The authors declare no competing financial interest.

ACKNOWLEDGMENTS

Y.D. acknowledges the Sloan Foundation for the Sloan Research Fellowship in Chemistry and 3M Nontenured Faculty Award that supported this work. H.C. acknowledges the Glenn E. and Barbara R. Ullyot Graduate Fellowship and the A.T. Widiger Fellowship. This work was conducted in part in the Frederick Seitz Materials Research Laboratory Central Facilities, G.L. Clark X-ray facility, and Beckman Institute for Advanced Science and Technology at the University of Illinois at Urbana Champaign. HT single-crystal structures were obtained at ChemMatCARS Sector, supported by the National Science Foundation under grant number NSF/CHE-1834750. Portions of this research were carried out at the Advanced Photon Source, a U.S. Department of Energy (DOE), Office of Science User Facility, operated for the DOE Office of Science by Argonne National Laboratory under Contract No. DE-AC02-06CH11357. We thank Dr. Jeffrey Alan Bertke for collecting and solving polymorphs of ditBu single crystals and Dr. Toby J. Woods for collecting and solving polymorphs of diTMS single crystals. We thank Dr. SuYin Grass Wang, Dr. YuSheng Chen, and Tieyan Chang for help setting up the HT SCXRD experiments. N.S. and P.C. thank the Cornell Institute for Computational Science and Engineering (ICSE) and the Maryland Advanced Research Computing Center (MARCC), which is partially funded by the State of Maryland, for provision of extensive computational resources. Y.H.G. is thankful to the Belgian National Fund for Scientific Research (FNRS) for financial support through research projects BTBT no. 2.4565.11, Phasetrans no. T.0058.14, Pi-Fast no. T.0072.18, and 2Dto3D no. 30489208. Financial supports from the French Community of Belgian (ARC no. 20061) and by the Walloon Region (WCS no. 1117306, SOLIDYE no. 1510602) are also acknowledged.

REFERENCES

- (1) Bernstein, J. Polymorphism in Molecular Crystals; Oxford University Press: OxfordClarendon Press: New York, USA, 2002.
- (2) Sutton, C.; Risko, C.; Brédas, J.-L. Noncovalent Intermolecular Interactions in Organic Electronic Materials: Implications for the Molecular Packing vs Electronic Properties of Acenes. *Chem. Mater.* **2016**, 28, 3–16.
- (3) Cruz-Cabeza, A. J.; Reutzel-Edens, S. M.; Bernstein, J. Facts and fictions about polymorphism. *Chem. Soc. Rev.* 2015, 44, 8619–8635.

(4) Gentili, D.; Gazzano, M.; Melucci, M.; Jones, D.; Cavallini, M. Polymorphism as an additional functionality of materials for technological applications at surfaces and interfaces. *Chem. Soc. Rev.* **2019**, *48*, 2502–2517.

- (5) Chung, H.; Diao, Y. Polymorphism as an emerging design strategy for high performance organic electronics. *J. Mater. Chem. C* **2016**, *4*, 3915–3933.
- (6) Jurchescu, O. D.; Mourey, D. A.; Subramanian, S.; Parkin, S. R.; Vogel, B. M.; Anthony, J. E.; Jackson, T. N.; Gundlach, D. J. Effects of polymorphism on charge transport in organic semiconductors. *Phys. Rev. B* **2009**, *80*, 085201.
- (7) Diao, Y.; Lenn, K. M.; Lee, W.-Y.; Blood-Forsythe, M. A.; Xu, J.; Mao, Y.; Kim, Y.; Reinspach, J. A.; Park, S.; Aspuru-Guzik, A.; Xue, G.; Clancy, P.; Bao, Z.; Mannsfeld, S. C. B. Understanding Polymorphism in Organic Semiconductor Thin Films through Nanoconfinement. J. Am. Chem. Soc. 2014, 136, 17046—17057.
- (8) Hiszpanski, A. M.; Baur, R. M.; Kim, B.; Tremblay, N. J.; Nuckolls, C.; Woll, A. R.; Loo, Y.-L. Tuning Polymorphism and Orientation in Organic Semiconductor Thin Films via Post-deposition Processing. J. Am. Chem. Soc. 2014, 136, 15749–15756.
- (9) Chen, J.; Shao, M.; Xiao, K.; Rondinone, A. J.; Loo, Y.-L.; Kent, P. R. C.; Sumpter, B. G.; Li, D.; Keum, J. K.; Diemer, P. J.; Anthony, J. E.; Jurchescu, O. D.; Huang, J. Solvent-type-dependent polymorphism and charge transport in a long fused-ring organic semiconductor. *Nanoscale* **2014**, *6*, 449–456.
- (10) He, T.; Stolte, M.; Burschka, C.; Hansen, N. H.; Musiol, T.; Kalblein, D.; Pflaum, J.; Tao, X. T.; Brill, J.; Wurthner, F. Single-crystal field-effect transistors of new Cl-2-NDI polymorph processed by sublimation in air. *Nat. Commun.* **2015**, *6*, 5954.
- (11) Stevens, L. A.; Goetz, K. P.; Fonari, A.; Shu, Y.; Williamson, R. M.; Brédas, J.-L.; Coropceanu, V.; Jurchescu, O. D.; Collis, G. E. Temperature-Mediated Polymorphism in Molecular Crystals: The Impact on Crystal Packing and Charge Transport. *Chem. Mater.* 2015, 27, 112–118.
- (12) He, P.; Tu, Z.; Zhao, G.; Zhen, Y.; Geng, H.; Yi, Y.; Wang, Z.; Zhang, H.; Xu, C.; Liu, J.; Lu, X.; Fu, X.; Zhao, Q.; Zhang, X.; Ji, D.; Jiang, L.; Dong, H.; Hu, W. Tuning the Crystal Polymorphs of Alkyl Thienoacene via Solution Self-Assembly Toward Air-Stable and High-Performance Organic Field-Effect Transistors. *Adv. Mater.* **2015**, 27, 825–830.
- (13) Purdum, G. E.; Yao, N.; Woll, A.; Gessner, T.; Weitz, R. T.; Loo, Y.-L. Understanding Polymorph Transformations in Core-Chlorinated Naphthalene Diimides and their Impact on Thin-Film Transistor Performance. *Adv. Funct. Mater.* **2016**, *26*, 2357–2364.
- (14) Chen, J.; Shao, M.; Xiao, K.; He, Z.; Li, D.; Lokitz, B. S.; Hensley, D. K.; Kilbey, S. M.; Anthony, J. E.; Keum, J. K.; Rondinone, A. J.; Lee, W.-Y.; Hong, S.; Bao, Z. Conjugated Polymer-Mediated Polymorphism of a High Performance, Small-Molecule Organic Semiconductor with Tuned Intermolecular Interactions, Enhanced Long-Range Order, and Charge Transport. *Chem. Mater.* **2013**, 25, 4378–4386.
- (15) Sorli, J. C.; Ai, Q.; Granger, D. B.; Gu, K.; Parkin, S.; Jarolimek, K.; Telesz, N.; Anthony, J. E.; Risko, C.; Loo, Y.-L. Impact of Atomistic Substitution on Thin-Film Structure and Charge Transport in a Germanyl-ethynyl Functionalized Pentacene. *Chem. Mater.* **2019**, *31*, *6615*.
- (16) Mnyukh, Y. Fundamentals of Solid-State Phase Transitions, Ferromagneticism and Ferroelectricity; Authorhouse: Indiana, USA, 2001.
- (17) Mnyukh, Y. Mechanism and kinetics of phase transitions and other reactions in solids. *Am. J. Condens. Matter Phys.* **2013**, *3*, 89–103.
- (18) Dunitz, J. D. Phase-Transitions in Molecular-Crystals from a Chemical Viewpoint. *Pure Appl. Chem.* **1991**, *63*, 177–185.
- (19) Garcia-Garibay, M. A. Molecular Crystals on the Move: From Single-Crystal-to-Single-Crystal Photoreactions to Molecular Machinery. *Angew. Chem., Int. Ed.* **2007**, *46*, 8945–8947.

- (20) Jiang, Q.; Shtukenberg, A. G.; Ward, M. D.; Hu, C. Non-Topotactic Phase Transformations in Single Crystals of β -Glycine. Cryst. Growth Des. **2015**, 15, 2568–2573.
- (21) Ito, H.; Muromoto, M.; Kurenuma, S.; Ishizaka, S.; Kitamura, N.; Sato, H.; Seki, T. Mechanical stimulation and solid seeding trigger single-crystal-to-single-crystal molecular domino transformations. *Nat. Commun.* **2013**, *4*, 2009.
- (22) Krishnan, B. P.; Sureshan, K. M. A Spontaneous Single-Crystal-to-Single-Crystal Polymorphic Transition Involving Major Packing Changes. J. Am. Chem. Soc. 2015, 137, 1692–1696.
- (23) Liu, G.; Liu, J.; Liu, Y.; Tao, X. Oriented Single-Crystal-to-Single-Crystal Phase Transition with Dramatic Changes in the Dimensions of Crystals. J. Am. Chem. Soc. 2014, 136, 590–593.
- (24) Chung, H.; Dudenko, D.; Zhang, F. J.; D'Avino, G.; Ruzie, C.; Richard, A.; Schweicher, G.; Cornil, J.; Beljonne, D.; Geerts, Y.; Diao, Y. Rotator side chains trigger cooperative transition for shape and function memory effect in organic semiconductors. *Nat. Commun.* **2018**, *9*, 278.
- (25) Nishiyama, Z. Martensitic Transformation; Elsevier: New York, USA, 2012.
- (26) Bhattacharya, K.; Conti, S.; Zanzotto, G.; Zimmer, J. Crystal symmetry and the reversibility of martensitic transformations. *Nature* **2004**, 428, 55–59.
- (27) Karothu, D. P.; Weston, J.; Desta, I. T.; Naumov, P. Shape-Memory and Self-Healing Effects in Mechanosalient Molecular Crystals. *J. Am. Chem. Soc.* **2016**, *138*, 13298–13306.
- (28) Yao, Z.-S.; Mito, M.; Kamachi, T.; Shiota, Y.; Yoshizawa, K.; Azuma, N.; Miyazaki, Y.; Takahashi, K.; Zhang, K.; Nakanishi, T.; Kang, S.; Kanegawa, S.; Sato, O. Molecular motor-driven abrupt anisotropic shape change in a single crystal of a Ni complex. *Nat. Chem.* **2014**, *6*, 1079–1083.
- (29) Su, S.-Q.; Kamachi, T.; Yao, Z.-S.; Huang, Y.-G.; Shiota, Y.; Yoshizawa, K.; Azuma, N.; Miyazaki, Y.; Nakano, M.; Maruta, G.; Takeda, S.; Kang, S.; Kanegawa, S.; Sato, O. Assembling an alkyl rotor to access abrupt and reversible crystalline deformation of a cobalt(II) complex. *Nat. Commun.* **2015**, *6*, 8810.
- (30) Das, D.; Jacobs, T.; Barbour, L. J. Exceptionally large positive and negative anisotropic thermal expansion of an organic crystalline material. *Nat. Mater.* **2010**, *9*, 36–39.
- (31) Skoko, Z.; Zamir, S.; Naumov, P.; Bernstein, J. The Thermosalient Phenomenon. "Jumping Crystals" and Crystal Chemistry of the Anticholinergic Agent Oxitropium Bromide. *J. Am. Chem. Soc.* **2010**, *132*, 14191–14202.
- (32) Panda, M. K.; Runčevski, T.; Chandra Sahoo, S.; Belik, A. A.; Nath, N. K.; Dinnebier, R. E.; Naumov, P. Colossal positive and negative thermal expansion and thermosalient effect in a pentamorphic organometallic martensite. *Nat. Commun.* **2014**, *5*, 4811.
- (33) Takamizawa, S.; Miyamoto, Y. Superelastic Organic Crystals. *Angew. Chem., Int. Ed.* **2014**, *53*, 6970–6973.
- (34) Sato, O. Dynamic molecular crystals with switchable physical properties. *Nat. Chem.* **2016**, *8*, 644–656.
- (35) Khalil, A.; Karothu, D. P.; Naumov, P. Direct Quantification of Rapid and Efficient Single-Stroke Actuation by a Martensitic Transition in a Thermosalient Crystal. *J. Am. Chem. Soc.* **2019**, *141*, 3371–3375.
- (36) Naumov, P.; Chizhik, S.; Panda, M. K.; Nath, N. K.; Boldyreva, E. Mechanically Responsive Molecular Crystals. *Chem. Rev.* **2015**, 115, 12440–12490.
- (37) Chung, H.; Ruzié, C.; Geerts, Y.; Diao, Y. Hybrid Mechanism of Nucleation and Cooperative Propagation in a Single-Crystal-to-Single-Crystal Transition of a Molecular Crystal. *Cryst. Growth Des.* **2018**, *18*, 4245–4251.
- (38) Devarapalli, R.; Kadambi, S. B.; Chen, C.-T.; Krishna, G. R.; Kammari, B. R.; Buehler, M. J.; Ramamurty, U.; Reddy, C. M. Remarkably Distinct Mechanical Flexibility in Three Structurally Similar Semiconducting Organic Crystals Studied by Nanoindentation and Molecular Dynamics. *Chem. Mater.* **2019**, *31*, 1391–1402.
- (39) Krishna, G. R.; Devarapalli, R.; Lal, G.; Reddy, C. M. Mechanically Flexible Organic Crystals Achieved by Introducing

Weak Interactions in Structure: Supramolecular Shape Synthons. J. Am. Chem. Soc. 2016, 138, 13561–13567.

- (40) Schweicher, G.; Lemaur, V.; Niebel, C.; Ruzié, C.; Diao, Y.; Goto, O.; Lee, W. Y.; Kim, Y.; Arlin, J. B.; Karpinska, J.; Kennedy, A. R.; Parkin, S. R.; Olivier, Y.; Mannsfeld, S. C. B.; Cornil, J.; Geerts, Y. H.; Bao, Z. Bulky End-Capped [1]Benzothieno[3,2-b]benzothiophenes: Reaching High-Mobility Organic Semiconductors by Fine Tuning of the Crystalline Solid-State Order. *Adv. Mater.* 2015, 27, 3066–3072.
- (41) Deegan, R. D.; Bakajin, O.; Dupont, T. F.; Huber, G.; Nagel, S. R.; Witten, T. A. Capillary flow as the cause of ring stains from dried liquid drops. *Nature* **1997**, *389*, 827–829.
- (42) Larkin, P. J.; Dabros, M.; Sarsfield, B.; Chan, E.; Carriere, J. T.; Smith, B. C. Polymorph Characterization of Active Pharmaceutical Ingredients (APIs) Using Low-Frequency Raman Spectroscopy. *Appl. Spectrosc.* **2014**, *68*, 758–776.
- (43) Brillante, A.; Bilotti, I.; Della Valle, R. G.; Venuti, E.; Masino, M.; Girlando, A. Characterization of phase purity in organic semiconductors by lattice-phonon confocal Raman mapping: Application to pentacene. *Adv. Mater.* 2005, *17*, 2549.
- (44) Macrae, C. F.; Bruno, I. J.; Chisholm, J. A.; Edgington, P. R.; McCabe, P.; Pidcock, E.; Rodriguez-Monge, L.; Taylor, R.; van de Streek, J.; Wood, P. A. Mercury CSD 2.0 new features for the visualization and investigation of crystal structures. *J. Appl. Crystallogr.* **2008**, *41*, 466–470.
- (45) Bondi, A. van der Waals Volumes and Radii. J. Phys. Chem. 1964, 68, 441-451.
- (46) Purdum, G. E.; Telesz, N. G.; Jarolimek, K.; Ryno, S. M.; Gessner, T.; Davy, N. C.; Petty, A. J.; Zhen, Y.; Shu, Y.; Facchetti, A.; Collis, G. E.; Hu, W.; Wu, C.; Anthony, J. E.; Weitz, R. T.; Risko, C.; Loo, Y.-L. Presence of Short Intermolecular Contacts Screens for Kinetic Stability in Packing Polymorphs. J. Am. Chem. Soc. 2018, 140, 7519—7525.
- (47) Rao, R.; Sakuntala, T.; Deb, S. K. Order-disorder transition in triethylenediamine: A Raman scattering study. *J. Mol. Struct.* **2006**, 789, 195–199.
- (48) Giri, G.; Verploegen, E.; Mannsfeld, S. C. B.; Atahan-Evrenk, S.; Kim, D. H.; Lee, S. Y.; Becerril, H. A.; Aspuru-Guzik, A.; Toney, M. F.; Bao, Z. Tuning charge transport in solution-sheared organic semiconductors using lattice strain. *Nature* **2011**, *480*, 504–508.